Near-field spectroscopy of silicon dioxide thin films

L. M. Zhang,[1] G. O. Andreev,[2] Z. Fei,[2] A. S. McLeod,[2] G. Dominguez,[3] M. Thiemens,[3] A. H. Castro-Neto,[4]
D. N. Basov,[2] and M. M. Fogler[2]

[1]*Department of Physics, Boston University, 590 Commonwealth Avenue, Boston, Massachusetts 02215, USA*
[2]*Department of Physics, University of California San Diego, 9500 Gilman Drive, La Jolla, California 92093, USA*
[3]*Department of Chemistry, University of California San Diego, 9500 Gilman Drive, La Jolla, California 92093, USA*
[4]*Graphene Research Centre and Department of Physics, National University of Singapore, 2 Science Drive 3, 117542, Singapore*

We analyze the results of scanning near-field infrared spectroscopy performed on thin films of a-SiO$_2$ on Si substrate. The measured near-field signal exhibits surface-phonon resonances whose strength has a prominent thickness dependence in the range from 2 to 300 nm. These observations are compared with calculations in which the tip of the near-field infrared spectrometer is modeled either as a point dipole or an elongated spheroid. The latter model accounts for the antenna effect of the tip and gives a better agreement with the experiment. Possible applications of the near-field technique for depth profiling of layered nanostructures are discussed.

I. INTRODUCTION

Scattering scanning near-field optical microscopy (s-SNOM)[1–3] is a powerful tool for probing local electromagnetic response of diverse materials. The s-SNOM achieves spatial resolution of 10–20 nm, which is especially valuable in the physically interesting infrared region[4,5] where the resolution of conventional spectroscopy is fundamentally limited by a rather large wavelength $\lambda \sim 5$–$500\,\mu$m. The s-SNOM techniques have been rapidly advancing,[6,7] which enabled their applications to imaging spectroscopy of complex oxides,[8–14] organic monolayers,[15] and graphene.[16]

The s-SNOM utilizes scattering of incident light by the tip of an atomic force microscope (AFM) positioned next to the probed sample (Fig. 1). The tip couples to the sample via evanescent waves of large in-plane momenta $q \sim 1/a$, where a is the tip radius of curvature (a few tens of nanometers). This is why the lateral resolution of the s-SNOM is determined primarily by a rather than λ.[17–19] (This property is quite general and holds for other tip-enhanced near-field techniques, e.g., scanning impedance microscopy[20] and inelastic light scattering.[21,22])

One of the interesting open questions is the depth (z-coordinate) resolution of the s-SNOM probes. Previous experiments suggested that it is comparable to the lateral resolution $\sim a$, based on imaging of small subsurface particles.[23] In this paper we report near-field measurements of SiO$_2$ thin films which demonstrate that films as thick as several hundred nanometers have a response clearly different from that of the bulk material. Thus, if instead of particles the sample is made of layers, then the s-SNOM is able to detect them at much larger depths.

We compare our experimental results with two theoretical models, the conventional point-dipole approximation[1,24] and the spheroidal model. The former is very simple to implement but is also very crude. Predictably, it yields a bulk-like response of the s-SNOM signal as soon as the SiO$_2$ film thickness exceeds the tip radius, in disagreement with the experiment.

A plausible reason for shortcomings of the point-dipole model is its failure to account for the strongly elongated shape of the tip. Such a tip acts as an optical antenna[1–3] that greatly enhances the electric field inside the tip-sample nanogap. Existing analytical models[25,26] that attempt to treat elongated tips are not suitable for layered substrates. This compels us to study the problem numerically.

To make the calculations tractable, we follow examples in the literature[27–29] and model the tip as a metallic spheroid of total length $2L \gg a$, see Fig. 1. As shown below, this gives results in a much better agreement with the experiment in terms of both the frequency and the thickness dependence of the near-field signal. We attribute the origin of the more gradual film-thickness dependence in the spheroidal model to the aforementioned antenna effect. The magnitude of this effect is determined by the material response over length scales ranging from a to $2L$, and so it truly saturates only when the film thickness becomes much larger than $2L$.

The remainder of the paper is organized as follows. In Sec. II we summarize the experimental procedures and results. In Secs. III and IV we discuss the two theoretical models and compare their predictions with the measurements. Concluding remarks are given in Sec. V.

II. EXPERIMENT

In this section we summarize our experimental procedures and the results. We investigated commercially available calibration gratings, which contain strips or islands of SiO$_2$ thermally grown on Si, see the insets in Fig. 2(a). The manufacturer specified thicknesses of the SiO$_2$ layer spanned the range $d_1 = 2$, 18, 22, 108, and 300 nm. A combination of CO$_2$ and tunable quantum cascade lasers (DAYLIGHT SOLUTIONS) allowed us to cover the frequency range 890–1250 cm^{-1}. The near-field data were collected using a NEASPEC system.

The measured s-SNOM signal represents the electromagnetic field backscattered by the probe and the scanned sample. The complex amplitude $s(\omega,t)$ of the backscattered field varies periodically with the tapping frequency $\Omega \sim 40$ kHz as the distance $z_{\rm tip}$ between the sample and the nearest point of the tip undergoes harmonic oscillations

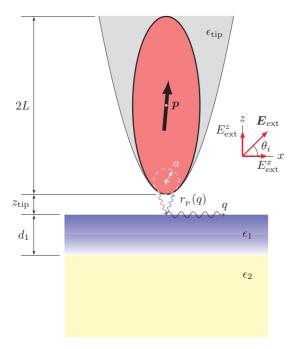$$z_{\rm tip}(t) = z_0 + \Delta z \, (1 - \cos \Omega t), \qquad (1)$$

FIG. 1. (Color online) Schematics of an s-SNOM experiment. A scanned probe, modeled as a metallic spheroid of length $2L$ and the apex curvature radius a, is positioned distance z_{tip} above the sample. The sample contains a film of thickness d_1 and dielectric function ϵ_1 on a substrate with dielectric function ϵ_2. The system is illuminated by infrared field $\mathbf{E}_{ext}$ at an angle of incidence θ. Scattering of this radiation by the tip creates evanescent waves with in-plane momenta $q \sim 1/a$. The experiment measures the total radiating dipole p of tip, which is determined by multiple reflections of the evanescent waves between the tip and sample. The reflections off the sample are characterized by the coefficient $r_P(q, \omega)$.

where $\Delta z \approx 50$ nm, typically. In order to suppress unwanted background and isolate the part of the signal scattered by the probe tip, the signal is demodulated. Namely, we extracted the absolute values $s_n(\omega)$ and phases $\phi_n(\omega)$ at tapping harmonics

$$s_n e^{i\phi_n} = \int_0^T \frac{dt}{T} e^{in\Omega t} s(\omega, t), \quad T = \frac{2\pi}{\Omega}. \tag{2}$$

The experimental results for the third harmonic s_3 are shown in Fig. 2(a). Each spectral data point in the main panel of Fig. 2(a) was extracted from s-SNOM images that were acquired at a fixed frequency ω of the tunable laser. A representative s-SNOM image is shown in the inset ii of Fig. 2(a). The imaged area was chosen such that it contained Si and SiO_2 regions identified from the simultaneously acquired AFM topography images, see the inset i of Fig. 2(a). The data points in the main panel of Fig. 2(a) represent the normalized amplitude $s_3(SiO_2)/s_3(Si)$, where $s_3(SiO_2)$ and $s_3(Si)$ are the raw third-order demodulation signals averaged over the entire SiO_2 and Si areas, respectively. The statistical uncertainty of these averaged data traces is about 2%.

The measured z_0 dependence of s_3 (the approach curves) is shown in Fig. 2(d). It was recorded while the setpoint of the tip oscillations was gradually moved either toward or away from the sample. The point of the tip-sample contact $z_0 = 0$ was assumed to coincide with the largest observed s_3. [The spectra shown in Fig. 2(a) correspond to this condition.] The

data at smaller tip-sample distances were discarded to avoid contamination of the third harmonic of the s-SNOM signal by mechanical rather than optical interaction between the tip and the sample. This procedure is convenient in practice but has a drawback that an error in identifying the contact point causes the approach curve to be shifted by some constant. We estimate this error not to exceed ~ 1 nm in most cases, where the approach curve rapidly and monotonically decays with z_0. Our results are in a qualitative agreement with a previous experimental study,[23] which reported approach curves for SiO_2 for a few discrete frequencies and film thicknesses.

For each studied SiO_2 thickness d_1, the normalized amplitude $s_3(SiO_2)/s_3(Si)$ exhibits a clear maximum at $\omega \approx 1130$ cm^{-1}. A trace of this resonance can be reliably identified even for $d_1 = 2$ nm sample. The key aspect of the data is a rapid decrease in the normalized amplitude of the main maximum as the thickness is reduced. Another notable feature is the growing strength and frequency shift of the secondary peaks on the high-ω side of the main peak as d_1 is decreased.

Since the response of Si is ω independent in our experimental range, the frequency dependence of the spectra in Fig. 2(a) originates from that of SiO_2. We attribute the maxima of $s_3(SiO_2)/s_3(Si)$ to the phonon modes localized at the air-SiO_2 interface.[6] These resonances occur in the frequency region between the bulk transverse and longitudinal modes of SiO_2 (the outer dashed lines in Fig. 3 below).

The results of our theoretical calculations for the normalized scattering amplitude are presented in the remaining panels of Fig. 2. They are discussed in the following sections.

III. RESPONSE FUNCTIONS AND COLLECTIVE MODES

The sample is modeled as a two-layer system. The first layer with dielectric function $\epsilon_1(\omega)$ occupies the slab $-d_1 < z < 0$. The second layer with dielectric function $\epsilon_2(\omega)$ occupies the half-space $z < -d_1$. The half-space $z > 0$ ("layer 0") is filled with air (dielectric constant $\epsilon_0 = 1$). The fundamental response functions of the system are the reflection coefficients $r_X(q, \omega)$, which are functions of in-plane momentum q, frequency ω, and polarization $X = S$ or P. The domain of definition of $r_X(q, \omega)$ is understood to include nonradiative modes $q > \sqrt{\epsilon_0}\, \omega/c$. It is known from previous studies that the s-SNOM signal is dominated by the P-polarized waves. In our two-layer model their reflection coefficient is given by a Fresnel-like formula

$$r_P(q, \omega) = \frac{\epsilon_* k_0^z - \epsilon_0 k_1^z}{\epsilon_* k_0^z + \epsilon_0 k_1^z}, \tag{3}$$

$$\epsilon_*(q, \omega) = \epsilon_1 \frac{\epsilon_2 k_1^z - \epsilon_1 k_1^z \tanh i k_1^z d_1}{\epsilon_1 k_2^z - \epsilon_2 k_1^z \tanh i k_1^z d_1}, \tag{4}$$

where z-axis momenta k_j^z are defined by

$$k_j^z = \sqrt{\epsilon_j \frac{\omega^2}{c^2} - q^2}, \quad \operatorname{Im} k_j^z \geqslant 0. \tag{5}$$

Equation (3) is valid for arbitrary q. In the near-field case where q is large and $k_j^z \simeq iq$, it simplifies to

$$r_P(q, \omega) \simeq \frac{\epsilon_* - \epsilon_0}{\epsilon_* + \epsilon_0}, \quad \epsilon_* \simeq \epsilon_1 \frac{\epsilon_2 + \epsilon_1 \tanh q d_1}{\epsilon_1 + \epsilon_2 \tanh q d_1}. \tag{6}$$
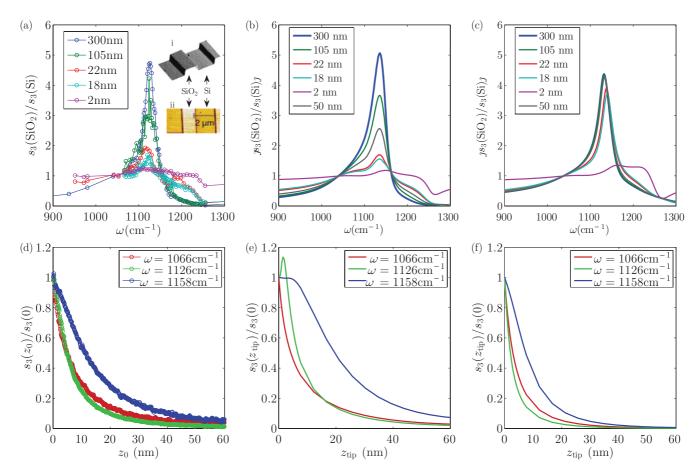
FIG. 2. (Color online) (a) Main panel: measured infrared near-field spectra for several SiO_2 film thicknesses. The quantity plotted is the absolute value s_3 of the third harmonic of the scattering amplitude normalized by that for the Si wafer. Inset i: a topographic AFM image of a region of an 18-nm sample. Inset ii: a near-field image of the same region acquired near the peak frequency $\omega \approx 1130\,cm^{-1}$. (b) Theoretical results for the spheroid model with $a = 30$ nm and $L = 15a$. (c) Theoretical results for the point-dipole model with $a = 30$ nm and $b = 0.75a$. (d) Measured approach curves for the 105-nm thick SiO_2. Note that z_0 is determined up to an additive constant ~ 1 nm (see text). (e) Calculated approach curve for the spheroid model. (f) The same for point-dipole model.

Assuming all ϵ_j are q independent, the effective dielectric function $\epsilon_*(q,\omega)$ depends on q only via the product qd_1 in this limit. Therefore, $r_p(q,\omega)$ for one thickness d_1 can be obtained from another by rescaling q. As discussed in Sec. I and shown in more detail below, the most important momenta are $q \sim 1/a$ where $a \sim 30$ nm is the tip radius. Therefore, we can get an approximate understanding of the system response by examining the behavior of $r_p(q,\omega)$ as a function of ω at fixed $qd_1 \sim d_1/a$. This behavior is dictated by the spectrum of surface collective modes, as follows.

In general, surface modes correspond to poles of the response functions r_X. Function r_p given by Eq. (6) can have up to two poles at each qd_1 (see, e.g., Ref. 30). They are defined by the following condition on $\epsilon_1(\omega)$:

$$\epsilon_1(\omega) = -\frac{\epsilon_0 + \epsilon_2}{2\tanh qd_1} \pm \sqrt{\frac{(\epsilon_0 + \epsilon_2)^2}{4\tanh^2 qd_1} - \epsilon_0\epsilon_2}. \qquad (7)$$

At large qd_1, where $\tanh qd_1 = 1$, this condition yields $\epsilon_1(\omega) = -\epsilon_0$ or $\epsilon_1(\omega) = -\epsilon_2$, which correspond to modes localized at the upper 0–1 and the lower 1–2 interfaces, respectively. Actually, the latter "pole" has vanishingly small

residue because evanescent waves do not reach the lower interface at $qd_1 = \infty$. There is no q dispersion and no coupling of the two modes in this limit. The dispersion appears at finite qd_1, where the two modes become mixed. In particular, we find

$$\epsilon_1(\omega) \simeq -\frac{qd_1}{\epsilon_0^{-1} + \epsilon_2^{-1}} \qquad \text{``0–1''} \qquad (8a)$$

$$\simeq -\frac{\epsilon_0 + \epsilon_2}{qd_1} \qquad \text{``1–2''} \qquad (8b)$$

at $qd_1 \ll 1$. At finite q, both interfaces participate in generating these excitations. The labels "0–1" and "1–2" are for convenience: they indicate at which interface a given dispersion branch is ultimately localized as q increases. At $qd_1 = 0$, the 0–1 and 1–2 branches are characterized by $\epsilon_1(\omega) = 0$ and $\epsilon_1(\omega) = -\infty$, which correspond, respectively, to the bulk longitudinal and transverse phonon frequencies ω_{LO} and ω_{TO}.

If we try to apply this formalism to real materials, we face the problem that Eq. (7) has no solutions for real ω because the dielectric functions have finite imaginary parts. This is why in practice the collective mode spectra are usually defined differently. They are identified with the maxima of dissipation,
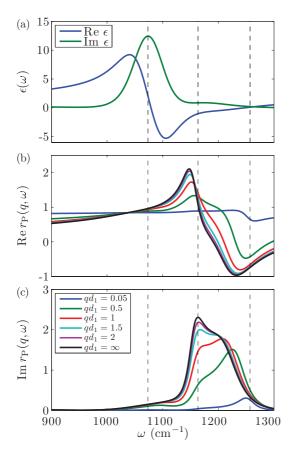
FIG. 3. (Color online) (a) Dielectric function of bulk SiO_2 as a function of frequency from ellipsometry. (b) The real and (c) the imaginary parts of the near-field reflection coefficient $r_p(q,\omega)$ for several qd_1. In all the panels three dashed lines indicate the transverse optical phonon frequency $\omega_{TO} \approx 1074$ cm^{-1}, the surface optical phonon frequency $\omega_{SP} \approx 1164$ cm^{-1}, and the longitudinal optical phonon frequency $\omega_{LO} \approx 1263$ cm^{-1}.

that is, $\mathrm{Im}\, r_p$. The number of these maxima can be fewer than the total allowed number of the modes because some of them can be overdamped. Similarly, we define ω_{LO} and ω_{TO} as the frequencies that correspond to the maxima of $-\mathrm{Im}\, \epsilon_1^{-1}(\omega)$ and $\mathrm{Im}\, \epsilon_1(\omega)$.

To see what kind of spectra are realized in our system, we use our ellipsometry data for $\epsilon_1(\omega)$ [Fig. 3(a)] and Eq. (6) to compute r_p for several values of qd_1. (The ellipsometry was done on $d_1 = 300$ nm sample.) The plot of these quantities as a function of ω is presented in Fig. 3(c). Three maxima on each curve in the region of primary interest $\omega > 1000$ cm^{-1} are apparent. They exist already at $qd_1 = \infty$, and so all of them belong to the upper (air-SiO_2) interface. In fact, we do not expect sharp modes at the lower (SiO_2-Si) interface because the dielectric function of Si is quite large $\epsilon_2 \approx 11.7$ in the studied range of ω. The lowest value of $\mathrm{Re}\, \epsilon_1 \approx -5.0$ is not sufficient to compensate ϵ_2 and generate 1–2 modes [cf. Eq. (7)].

The main peak of $\mathrm{Im}\, r_p$ at $qd_1 = \infty$ defines the surface phonon frequency of SiO_2 $\omega_{SP} \approx 1164$ cm^{-1}. There also exist secondary peaks at $\omega \approx 1100$ cm^{-1} and $\omega \approx 1220$ cm^{-1}. Their evolution as a function of qd_1 comply with the general scheme outlined above. As qd_1 decreases, all the three peaks

loose strength, as expected, because the volume of SiO_2 probed by the tip diminishes. The lower-ω secondary peak redshifts, moving toward ω_{TO}, and then quickly disappears. This agrees with the SiO_2-Si resonance being highly damped. The higher-ω secondary peak becomes dominant at $qd_1 < 0.5$ and demonstrates a systematic shift toward ω_{LO} [see Fig. 3(c)].

A notable feature of Fig. 3(b) is the clustering of the crossing points of the different curves near $\omega = 1036$ cm^{-1}. This is the frequency where the dielectric function of SiO_2 is the closest to that of Si, $\epsilon_2 \approx 11.7$. As a result, the two layers act almost as one bulk material, so that $r_p(\omega)$ is approximately thickness independent.

There is a qualitative correspondence between the features displayed by the reflection coefficient r_p and the observed near-field signal $s_3(SiO_2)/s_3(Si)$ [cf. Figs. 2(a), 3(b), and 3(c)]. However, the relation between $r_p(q,\omega)$ and the measured s-SNOM signal is nontrivial. For example, the frequency positions of the maxima in $\mathrm{Im}\, r_p(q,\omega)$ and those in $s_3(SiO_2)/s_3(Si)$ differ by as much as 40 cm^{-1}. We also suspect that there may be some slight differences between the optical constants of thick films we assume in our calculations and those of the small SiO_2 structures we probe by the s-SNOM. This is the likely reason why the crossing point of the experimental curves occurs near 1060 cm^{-1} rather than 1036 cm^{-1} predicted by both our models (cf. Fig. 2).

Developing a reliable procedure for inferring $r_p(q,\omega)$ from s_3 remains a challenge for the theory. The next section presents our current approach toward this ultimate goal.

IV. TIP-SAMPLE INTERACTION

Both radiative and nonradiative waves may play significant roles in the s-SNOM experiment.[27] The radiative modes magnify the signal by a certain far-field factor (FFF) $F(q_s,\omega)$, where

$$q_s = \frac{\omega}{c} \sin\theta \qquad (9)$$

is the momentum of these modes for the angle of incidence θ. The nonradiative modes influence the effective polarizability $\chi(\omega, z_{tip})$ of the tip, that is, the ratio of its dipole moment p^z and the external electric field E_{ext}^z. Altogether the demodulated s-SNOM signal $s_n e^{i\phi_n}$ can be written as

$$s_n e^{i\phi_n} \propto \chi_n E_{ext} \sin 2\theta\, F(q_s,\omega), \qquad (10)$$

$$\chi_n(\omega) = \int_0^T \frac{dt}{T} e^{in\Omega t} \chi(\omega, z_{tip}(t)). \qquad (11)$$

Below we discuss the FFF and the tip polarizability separately.

A. Far-field factor

The FFF takes into account that the total external field illuminating the tip consists of the incident wave and the wave reflected off the sample. Similarly, the dipole radiation of the tip reaches the detector in two ways: directly and after being reflected by the sample.[27,31,32] Therefore, the FFF is given by[31,33,34]

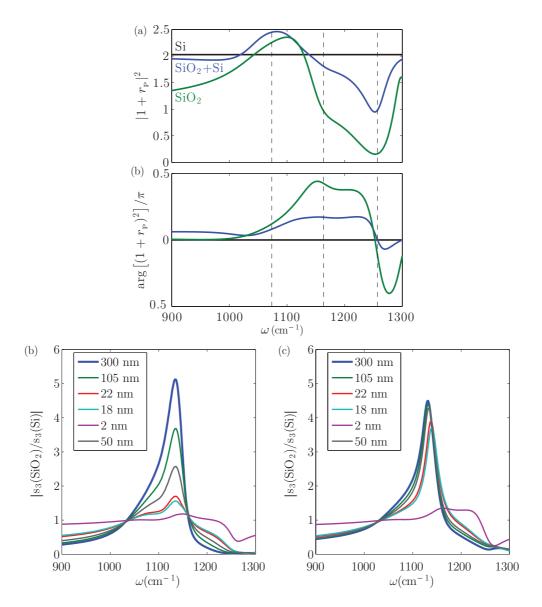$$F(q_s,\omega) = (1 + r_p)^2. \qquad (12)$$

FIG. 4. (Color online) (a) The absolute value and (b) the phase of the infinite-plane far-field factor computed as a function of frequency for the incidence angle $\theta = 45°$. The black trace is for bulk Si substrate, the blue one is for bulk SiO_2 substrate, the green one is for 300 nm thick SiO_2 followed by bulk Si. The meaning of the dashed lines is the same as in Fig. 3. (c) Same as Fig. 2(b) but with the far-field factor included. (d) Same as Fig. 2(c) but with the far-field factor included.

For a system in which all the layers are much wider than the wavelength, so that they can be considered effectively infinite in the x-y plane, the reflection coefficient in Eq. (12) is the usual Fresnel reflection coefficient computed including all the layers, $r_P = r_P(q_s, \omega)$. Previous s-SNOM experiments on systems of this type[32,34] have shown that the FFF may be an important part of the quantitative analysis. Conversely, there are reasons why in our case the FFF should not play much of a role.

First of all, in our samples SiO_2 layer occupies a minor fraction of the x-y plane forming small subwavelength regions. [These regions are shaped as either narrow stripes, cf. Fig. 2(a), or small squares.] Therefore, r_P in Eq. (12) should be nearly equal to the Fresnel reflection coefficient of the underlying Si substrate alone. Thus, the FFF should drop out from the ratio $s_3(SiO_2)/s_3(Si)$ plotted in Fig. 2.

Second, even if we willfully include the infinite-plane FFF in the calculation, it would produce only minor effects. Comparing Figs. 2(b) and 2(c) with Figs. 4(c) and 4(d) we see that the height of the main maximum would change by no more than 10% at all studied d_1. Actually, using the infinite-plane FFF produces features not present in the experimental data [Fig. 2(a)]. They include additional humps in $s_3(SiO_2)/s_3(Si)$ near $\omega_{TO} \approx 1074$ cm^{-1} and dips near $\omega_{LO} \approx 1272$ cm^{-1} [cf. Figs. 2(b) and 2(c)]. These features arise because the absolute value of the infinite-plane FFF has a maximum near ω_{TO} and a suppression near ω_{LO} [see Fig. 4(a)]. The main maximum of $s_3(SiO_2)/s_3(Si)$ is located at $\omega \approx 1030$ cm^{-1}, away from both ω_{TO} and ω_{LO}. This is why it is not greatly affected by the FFF.

These considerations imply that the observed strong d_1 dependence of the main peak in $s_3(SiO_2)/s_3(Si)$ is *not* due to the trivial far-field illumination effect. Accordingly, below
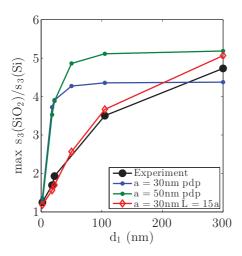
FIG. 5. (Color online) The thickness dependence of the s_3 peak for different tip models. The circles represent the point-dipole calculations, one for $a = 30$ nm (blue) and the other for $a = 50$ nm (green). The diamonds are for the spheroid model with $a = 30$ nm and $L = 15a$, the same as in Fig. 2(b). The black squares are derived from the experimental data shown in Fig. 2(a) after some smoothing over fluctuations.

we use the theoretical results of Figs. 2(b) and 2(c), which are computed without the FFF.

B. Point-dipole model of the tip

The effective tip polarizability $\chi(\omega, z_{tip})$ is the most important factor on the right-hand side of Eq. (10) and it is also the most difficult one to compute. This quantity is dictated by the near-field coupling between the tip and the sample. For irregular tip shapes it can be calculated only numerically. To reduce computational complexity, previous studies have also considered various regular shapes, for example, a spheroid,[27–29] a small sphere,[28,33,35–38] a rounded cone,[39] a "finite" dipole,[6,25] and a point dipole.[34,40,41] The actual tip shape in our experiments is close to a rounded pyramid.

The point-dipole approximation is the simplest one and it has been used extensively for modeling s-SNOM experiments, including those performed on multilayer systems.[16,34] The point-dipole model has two adjustable parameters: the polarizability a^3 of the effective dipole and its position b with respect to the bottom of the tip. The results obtained following the standard analysis[16,34] are shown in Fig. 2(c) using $a = 30$ nm and $b = 0.75a$. We see that even for this rather large a the point-dipole model does not reproduce the observed prominent dependence of s_3 on thickness at $d_1 > 22$ nm. (Such dependence cannot be reproduced even with unrealistically large $a = 50$ nm, see Sec. V.)

The discrepancy can be seen more clearly in Fig. 5, where the height of the peak in $s_3(SiO_2)/s_3(Si)$ corresponding to the surface phonon is plotted as a function of d_1. For the point-dipole model the curve flattens at $d_1 \sim b$. In contrast, the experimentally measured $s_3(SiO_2)/s_3(Si)$ maximum continues to rise with d_1. The point-dipole model also predicts a steeper than observed approach curves [Fig. 2(f)].

The physical origin of the saturation of the thickness dependence in Fig. 2(c) is easy to understand. One can think about the near-field coupling between the point dipole and the sample in terms of the method of images. For a dipole positioned at $z_{pd} = z_{tip} + b$, the image is concentrated at the depth z_{pd} below the surface. Therefore, films of thickness larger than z_{pd} would act as a bulk material. Another way to arrive at the same conclusion is to notice that the characteristic range of momenta of the relevant nonradiative waves is $q \lesssim 1/z_{pd}$. Since r_p depends on q through the term $\tanh q d_1$ [Eq. (6)], the dependence of the near-field coupling on d_1 should saturate at $d_1 \gtrsim z_{pd} \sim b$.

C. Spheroid model of the tip

The lack of saturation in the observed s-SNOM signal as a function of d_1 at $d_1 \gg a$ indicates that evanescent waves with momenta $q \ll 1/a$ also play a role in the near-field coupling between the tip and the sample. This is a signature of models in which the tip has a finite extent in space $2L \gg a$, see Fig. 1. Although such models are certainly more realistic than a point-dipole approximation, there has not been a systematic study of how the results would depend on the exact shape of the tip. Given some initial success of the point-dipole approximation, we speculate that a suitable simple shape can provide a good compromise between increase in computational effort and ability to capture relevant physics.

To test this idea, we modeled the tip as an elongated metallic spheroid positioned above a two-layer medium. This follows a tradition in the literature wherein similar models were considered[27–29] for the case of bulk substrates. In Ref. 25 an analytical formula for the spheroidal tip was also proposed, based on heuristic arguments. However, it cannot be easily extended to the q-dependent r_p we study here. Instead, our calculations are done numerically. They involve only two essential approximations. One is neglecting retardation, which is justified if the length $2L$ of the spheroid is smaller than λ. The other one is neglecting the finite skin depth of the metal (Pt-Ir alloy) covering the tip. Due to computational difficulties involved, this issue is left for future investigation.

The calculations were performed in two ways. First is the standard boundary-element method. In this method we divide the entire tip—assuming azimuthal symmetry—into a large number (typically 200) of small cylindrical segments. We assume that different segments interact by Coulomb interaction as coaxial rings. The interaction of each segment with itself is defined in such a way that the polarizability of the tip in the absence of the sample coincides with the known analytical result for the prolate spheroid. The effect of the sample is included by adding ring-ring interactions mediated by reflected electrostatic fields. This is accomplished by numerical quadrature over the product of $r_p(q, \omega)$ and suitable form factors. This is the most time-consuming step of the simulation. After the interaction kernel is generated in this way, it is straightforward to solve numerically for the dipole moment of the tip induced by a unit external field, which is the desired polarizability $\chi(\omega, z_{tip})$.

We also developed a second numerical method of computing χ (to be described elsewhere), based on an expansion of the electric field in ellipsoidal harmonics. This alternative method

is similar to that used for a metallic sphere above a dielectric half-space.[31,33] We verified that the two methods give identical results.

Substituting the computed tip polarizability χ into Eq. (10) and demodulating per Eq. (11), we obtain approach curves. Figure 2(e) illustrates that approach curves can be nonmonotonic near the resonances. This behavior has been reported by other experimental groups[23,41] but it was not anticipated when the experimental data were collected in this study. As explained in Sec. II, we followed a simplified procedure in which $z_0 = 0$ was assumed to be the point where the observed s_3 was the largest. The data points at shorter tip-sample separation were discarded. [In computing the s-SNOM amplitude presented in Fig. 2(b) s_3 we followed a similar procedure: we always chose z_{tip} that gave the largest s_3.] Normally this procedure can lead only to some small shift of the approach curves with respect to the true point of the tip-sample contact $z_0 = 0$. However, for nonmonotonic approach curves the shift of z_0 could be as large as several nanometers. This may be one reason for the lack of perfect agreement between Figs. 2(d) and 2(e). We leave a more careful investigation of the approach curves and their comparison with the calculations for future work. Arguably, the approach curves predicted by the spheroid model [Fig. 2(e)] are not as rapidly decaying with z_0 as those for the point-dipole model [Fig. 2(f)] and in this regard they better resemble the experimental observations [Fig. 2(d)].

The spheroid model has two adjustable parameters: the apex radius of curvature a and the half-length L. When $L = a$ the spheroid becomes a sphere. In this case the spheroid model gives results similar to the point-dipole model [i.e., Fig. 2(c)]. As the ratio L/a increases, the differences appear. However, once L/a exceeds ten, the normalized signal $s_3(\mathrm{SiO_2})/s_3(\mathrm{Si})$ does not change much at $d_1 \leqslant 300$ nm. Therefore, for long spheroids we effectively have a single adjustable parameter a. Remarkably, the thickness dependence of the s_3 peak for the spheroid model matches the experiment very well (Fig. 5).

V. CONCLUSIONS

In this paper we reported the results of scanning near-field optical spectroscopy of amorphous SiO_2 films grown on Si substrate. We discussed the collective mode spectra of such structures and compared measurements with two theoretical calculations. The first one is based on a conventional approximation in which the tip of the scanned probe is modeled

as a point dipole. In the second one the tip is treated as an elongated spheroid, which significantly improves agreement with the experiment.

We explain the qualitative difference between the two models as follows. An important physical ingredient missing in the point-dipole model is the enhancement of the electric field near the apex of the tip—the antenna effect. This phenomenon is well known from classical electrostatics. The enhancement of the field is controlled primarily by the ratio of the total length of the tip $2L$ (actually, the smaller of $2L$ and λ) and the apex radius of curvature $\sim a$ (Ref. 2). The point-dipole model has been successful in the past without this enhancement factor because of the normalization procedure. Instead of absolute s_n, one usually reports s_n normalized to some reference material such as Au or, in our case, Si. This way one eliminates any possible frequency dependence of the source radiation, but at the same time cancels the part of the signal scaling with tip size. For a stratified sample this cancellation is imperfect because the the field enhancement depends also on the dielectric response of the sample, which is a function of momentum q. For a tip of length $2L$, harmonics relevant for the field enhancement have momenta ranging from $q \sim 1/a$ down to $q \sim 1/L$. Therefore, one may expect that the dependence of the s-SNOM signal on the thickness d_1 of the top layer would saturate only when $d_1 \sim L$. Our simulations provide direct evidence for this claim.

Despite the important role of the $q \ll 1/a$ momenta, the lateral resolution of the s-SNOM remains of the order of the apex radius $\sim a$. Further theoretical work is required to better understand this observation.

In closing, the strong experimentally observed thickness dependence of the near-field signal indicates that s-SNOM is capable of not only high lateral resolution but can also probe the system in the third dimension. The response of layered systems is shown to be different from that of systems with small subsurface particles.[23] We hope that experimental and theoretical approaches presented in this paper may be of use for accurate depth profiling of various dielectric and metallic nanostructures.

[1] F. Keilmann and R. Hillenbrand, Philos. Trans. R. Soc. London Ser. A **362**, 787 (2004).

[2] L. Novotny and B. Hecht, *Principles of Nano-Optics* (Cambridge University Press, Cambridge, 2006).

[3] F. Keilmann and R. Hillenbrand, *Nano-Optics and Near-Field Optical Microscopy*, edited by A. Zayats and D. Richards (Artech House, Norwood, 2009), Chap. 11, pp. 235–266.

[4] D. N. Basov, R. D. Averitt, D. van der Marel, M. Dressel, and K. Haule, Rev. Mod. Phys. **83**, 471 (2011).

[5] D. N. Basov and A. V. Chubukov, Nat. Phys. **7**, 272 (2011).

[6] S. Amarie and F. Keilmann, Phys. Rev. B **83**, 045404 (2011).

[7] F. Huth, M. Schnell, J. Wittborn, N. Ocelic, and R. Hillenbrand, Nat. Mater. **10**, 352 (2011).

[8] H. Ma and J. Levy, Nano Lett. **6**, 341 (2006).

[9] M. M. Qazilbash, M. Brehm, B.-G. Chae, P.-C. Ho, G. O. Andreev, B.-J. Kim, S. J. Yun, A. V. Balatsky, M. B. Maple, F. Keilmann, H.-T. Kim, and D. N. Basov, Science **318**, 1750 (2007).

[10] H. Zhan, V. Astley, M. Hvasta, J. A. Deibel, D. M. Mittleman, and Y.-S. Lim, Appl. Phys. Lett. **91**, 162110 (2007).

[11] M. M. Qazilbash, M. Brehm, G. O. Andreev, A. Frenzel, P.-C. Ho, B.-G. Chae, B.-J. Kim, S. J. Yun, H.-T. Kim, A. V. Balatsky, O. G. Shpyrko, M. B. Maple, F. Keilmann, and D. N. Basov, Phys. Rev. B **79**, 075107 (2009).

[12] A. Frenzel, M. M. Qazilbash, M. Brehm, B.-G. Chae, B.-J. Kim, H.-T. Kim, A. V. Balatsky, F. Keilmann, and D. N. Basov, Phys. Rev. B **80**, 115115 (2009).

[13] A. C. Jones, S. Berweger, J. Wei, D. Cobden, and M. B. Raschke, Nano Lett. **10**, 1574 (2010),

[14] K. Lai, M. Nakamura, W. Kundhikanjana, M. Kawasaki, Y. Tokura, M. A. Kelly, and Z.-X. Shen, Science **329**, 190 (2010).

[15] M. P. Nikiforov, S. C. Kehr, T.-H. Park, P. Milde, U. Zerweck, C. Loppacher, L. M. Eng, M. J. Therien, N. Engheta, and D. Bonnell, J. Appl. Phys. **106**, 114307 (2009).

[16] Z. Fei, G. O. Andreev, W. Bao, L. M. Zhang, A. S. McLeod, C. Wang, M. K. Stewart, Z. Zhao, G. Dominguez, M. Thiemens, M. M. Fogler, M. J. Tauber, A. H. Castro Neto, C. N. Lau, F. Keilmann, and D. N. Basov, Nano Lett. **11**, 4701 (2011).

[17] K. Lai, M. B. Ji, N. Leindecker, M. A. Kelly, and Z. X. Shen, Rev. Sci. Instrum. **78**, 063702 (2007).

[18] A. J. Huber, F. Keilmann, J. Wittborn, J. Aizpurua, and R. Hillenbrand, Nano Lett. **8**, 3766 (2008), pMID: 18837565

[19] R. L. Olmon, P. M. Krenz, A. C. Jones, G. D. Boreman, and M. B. Raschke, Opt. Express **16**, 20295 (2008).

[20] K. Lai, H. Peng, W. Kundhikanjana, D. T. Schoen, C. Xie, S. Meister, Y. Cui, M. A. Kelly, and Z.-X. Shen, Nano Lett. **9**, 1265 (2009).

[21] Y. You, C. Du, Y. Ma, J. Kasim, T. Yu, and Z. Shen, Nanotechnology **19**, 395705 (2008).

[22] J. Stadler, T. Schmid, and R. Zenobi, ACS Nano **5**, 8442 (2011).

[23] T. Taubner, F. Keilmann, and R. Hillenbrand, Opt. Express **13**, 8893 (2005).

[24] R. Hillenbrand, T. Taubner, and F. Keilmann, Nature (London) **418**, 159 (2002).

[25] A. Cvitkovic, N. Ocelic, and R. Hillenbrand, Opt. Express **15**, 8550 (2007).

[26] K. Moon, E. Jung, M. Lim, Y. Do, and H. Han, Opt. Express **19**, 11539 (2011).

[27] J. A. Porto, P. Johansson, S. P. Apell, and T. López-Ríos, Phys. Rev. B **67**, 085409 (2003).

[28] J. Renger, S. Grafström, L. M. Eng, and R. Hillenbrand, Phys. Rev. B **71**, 075410 (2005).

[29] R. Esteban, R. Vogelgesang, and K. Kern, Opt. Express **17**, 2518 (2009).

[30] B. Prade, J. Y. Vinet, and A. Mysyrowicz, Phys. Rev. B **44**, 13556 (1991).

[31] G. Ford and W. Weber, Phys. Rep. **113**, 195 (1984).

[32] M. B. Raschke and C. Lienau, Appl. Phys. Lett. **83**, 5089 (2003).

[33] S. V. Sukhov, Ultramicroscopy **101**, 111 (2004).

[34] J. Aizpurua, T. Taubner, F. J. G. de Abajo, M. Brehm, and R. Hillenbrand, Opt. Express **16**, 1529 (2008).

[35] R. W. Rendell and D. J. Scalapino, Phys. Rev. B **24**, 3276 (1981).

[36] P. K. Aravind and H. Metiu, J. Phys. Chem. **86**, 5076 (1982).

[37] P. K. Aravind and H. Metiu, Surf. Sci. **124**, 506 (1983).

[38] R. Ruppin, Phys. Rev. B **45**, 11209 (1992).

[39] R. M. Roth, N. C. Panoiu, M. M. Adams, R. M. Osgood, C. C. Neacsu, and M. B. Raschke, Opt. Express **14**, 2921 (2006).

[40] R. Hillenbrand and F. Keilmann, Phys. Rev. Lett. **85**, 3029 (2000).

[41] T. Taubner, F. Keilmann, and R. Hillenbrand, Nano Lett. **4**, 1669 (2004).